# Pharmacological Evaluation of Enantiomers of AZ11645373 against the P2X7 Receptor

Andrew McGown,[a,b#] Nicolas Renault,[c#] Amélie Barczyk,[c] Jordan Nafie,[d] Luciano Barluzzi,[a] Daniel Guest,[a] Graham J. Tizzard,[e] Simon J. Coles,[e] David Leach,[f] Daniel von Emloh,[f] Léa Sutton,[f] Keira Bailey,[f] Lewis Edmunds,[f] Barnaby W. Greenland,[a] Regis Millet,[c,] John Spencer,[a,b*] Xavier Dezitter [c,*]

[a] Department of Chemistry, School of Life Sciences, University of Sussex, Falmer, BN1 9QJ, UK.

[b] Sussex Drug Discovery Centre, Department of Chemistry, School of Life Sciences, University of Sussex, Falmer, BN1 9QJ, UK.

[c] Univ. Lille, Inserm, CHU Lille, U1286 - INFINITE - Institute for Translational Research in Inflammation, F-59000 Lille, France.

[d] Biotools, Inc., 17546 Beeline Highway, Jupiter, Florida 33458, US.

[e] National Crystallography Service, School of Chemistry, University of Southampton, Southampton, SO17 1BJ, UK.

[f] Reach Separations Ltd, BioCity, Nottingham, Pennyfoot Street, Nottingham, NG1 1GF, UK.

[c] Univ. Lille, Inserm, CHU Lille, U1286 - INFINITE - Institute for Translational Research in Inflammation, F-59000 Lille, France.

[*] corresponding authors

[#] A.M. and N.R. contributed equally to this work

**Abstract**.

The P2X purinergic receptor 7 (P2X7) has an essential role in inflammation, innate immunity, tumor progression, neurodegenerative diseases, and several other diseases, leading subsequently to the development of P2X7 modulators. AZ11645373 is a frequently studied P2X7 antagonist tool compound, but always as a racemic mixture. Racemic AZ11645373 can be separated, into its respective enantiomers by chiral chromatography, albeit in small batches, and these were stereochemically intact over a year later, by chiral HPLC analysis. On a higher scale, significant decomposition is observed. One of the enantiomers was crystallised as a palladium complex and its *(R)*-configuration was determined by single crystal X-ray diffraction, further confirmed, in solution, by vibrational circular dichroism. Biological studies demonstrated that both (*S*)- and (*R*)-forms were able to fully inhibit human P2X7, but *(R)*-AZ11645373 was more potent, with an $IC_{50}$ of 32.9 nM. Contrary to its effect on human P2X7, *(S)*-AZ11645373 was ineffective on mouse P2X7, while the *(R)*-AZ11645373 enantiomer was a full antagonist. These results demonstrated that the antagonistic effects of racemic AZ11645373 are mainly due to its (*R*)-enantiomer. Site-directed mutagenesis and molecular dynamics simulations indicated that the *(R)*-enantiomer may form specific interactions with Phe95 and the antagonists bound to the other P2X7 monomers. Phe95 is situated at the channel pore and appears to be the pivotal molecular gateway between AZ11645373 allosteric binding and locking of the closed state of the P2X7 channel. All together, these structure-function relationships should be helpful for drug design of P2X7 modulators.

## INTRODUCTION.

The P2X purinergic receptor 7 (P2X7) is a poorly selective ATP-gated ion channel, expressed in many cell types, including immune cells (macrophages and microglia) and cells in the central and peripheral nervous

systems [1–3]. P2X7 has low affinity for extracellular ATP (mM range) and is activated in the presence of high levels of extracellular ATP as a result of inflammation or cell damage [4,5]. P2X7 signalling affects major cell functions and cell fate, including inflammation, proliferation, metabolism and cell death [4–6]. P2X7 is implicated in both physiological and pathophysiological processes such as inflammation, innate immunity, tumour progression, neurodegenerative disease, and several other diseases [1,3,6].

Functional P2X7 is formed by a complex of three monomers of 595 amino acids. Each monomer is composed of a short cytoplasmic N-terminal domain, an extracellular domain bearing the ATP binding site, two transmembrane helices, and a long C-terminal cytoplasmic domain. Upon ATP binding, the trimeric complex becomes rapidly permeable to cations, leading to $Ca^{2+}$ and $Na^{+}$ influx, and efflux of $K^{+}$. Sustained exposure to ATP induces the formation of a poorly selective membrane pore, termed the large pore, that allows the uptake of molecules of up to 900 Da in weight [5,7,8]. These plasma membrane events induce downstream intracellular signalling pathways that regulate different cellular functions, such as activation of the inflammasome, ROS production, regulation of metabolism, cytokine maturation and release leading to inflammation or cell proliferation [9,10]. Therefore, P2X7 presents as an emerging therapeutic target in the treatment of infectious and inflammatory diseases, neuropathic pain and cancers [1,3,5,11].

For several years, numerous structurally diverse antagonists have been developed with both improved affinity and selectivity towards P2X7 over other P2 receptor family members [3,6,12]. The binding mode of five antagonists was identified by crystallography of panda P2X7 and has revealed a common allosteric binding pocket, different from the ATP binding site, that is located between neighbouring monomers [13]. Binding of antagonists in the allosteric pocket impedes ATP-mediated P2X7 conformational changes and channel opening [13]. This was confirmed by site-directed mutagenesis and has provided significant insights into structure-activity relationships of P2X7 antagonists [13–16].

AZ11645373, developed by AstraZeneca, is one of the most used P2X7 antagonists in the literature. Its synthesis was first described in 2006 and its biological activity was fully determined on membrane currents, calcium influx, YO-PRO-1 uptake, IL1-β secretion in HEK and in THP-1 cells [17,18]. AZ11645373 is a highly potent and selective antagonist on human P2X7, with lower efficacy in rodents [17,19,20]. Its binding to the allosteric binding pocket of P2X7 was validated by site-directed mutagenesis accounting for the species differences in antagonistic activity [15]. AZ11645373 binding to P2X7 relies on aromatic interactions with Phe88, Phe103 and Phe95 and species differences are due to point mutations on Phe95, Phe108 and Val312. Actually, introduction of the homologous amino acids from the human P2X7 restore sensitivity of rat P2X7 to AZ11645373 [15]. However, AZ11645373 bears a chiral central carbon atom yet has always been used as a racemate. In this study, we sought to separate its enantiomers and to compare them to the racemate to further delve into structure-activity relationships (SAR).

## RESULTS AND DISCUSSION

P2X7 is an ion channel implicated in autoimmune and inflammatory diseases and neuropathic pain [1–3]. The antagonist AZ11645373 is an invaluable chemical tool for the P2X7 ion channel and pharmacological research, and is commercially available, albeit in racemic (*(R)-/(S)-*) form [17,18]. We wished to obtain it as separate enantiomers (Figure 1) since modelling suggested differential pharmacology and binding modes [15].

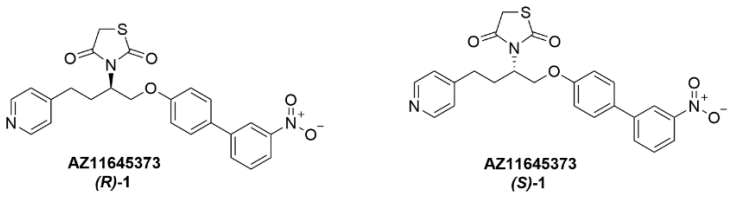


Figure 1. Enantiomers of **AZ11645373**.

Analytical chiral separation of a racemic sample of AZ11645373 was readily achieved and preparative chromatography was initially performed on a 100 mg scale. However, for structural and biological studies, we required larger quantities, and the subsequent separation was carried out on 3 g of commercially obtained racemic AZ11645373. Decomposition, reported, in the literature, to be the elimination of the thiazolidine-2,4-dione moiety [18], was observed when larger batches were subjected to purification, hence, small batches of *ca*. 100 mg each, were collected and carefully evaporated, and kept away from light. The separated fractions, with unknown absolute configuration, were initially termed fractions 1 and 2. Typically, enantiomeric excesses >95% were obtained (Figure 2). Batches kept in DMSO/$H_2O$, used for the ensuing biological assays, were re-assessed for chiral integrity, two years after initial chiral separation, and were still >95% ee (Supplementary Figure S1).

**Figure 2**

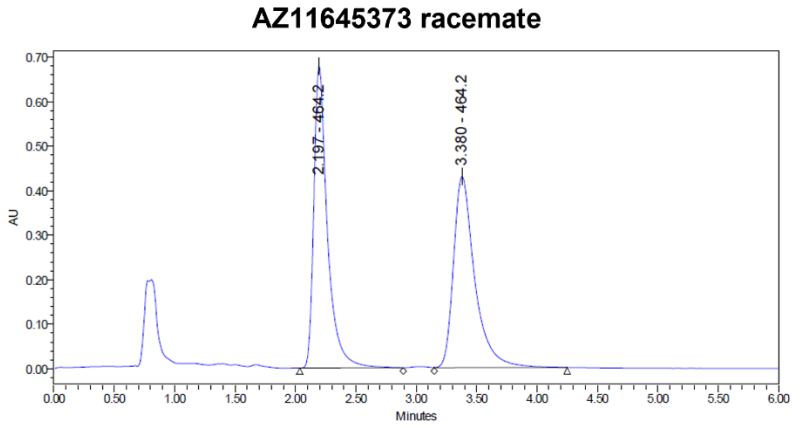


| | Retention Time (min) | Area (µV*sec) | % Area |
|---|---|---|---|
| 1 | 2.20 | 5272610 | 50.2 |
| 2 | 3.38 | 5240574 | 49.8 |

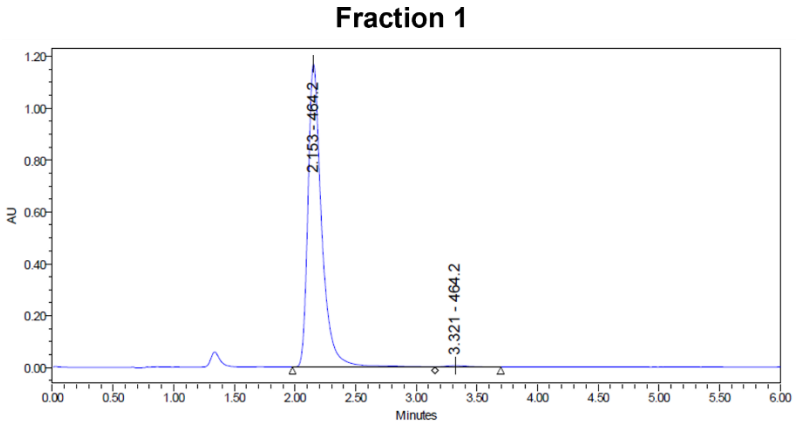


| | Retention Time (min) | Area (µV*sec) | % Area |
|---|---|---|---|
| 1 | 2.15 | 9162567 | 99.3 |
| 2 | 3.32 | 66087 | 0.7 |

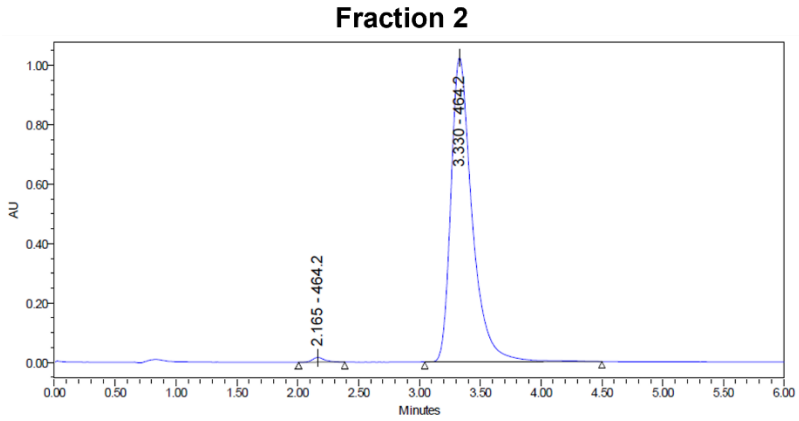


| | Retention Time (min) | Area (µV*sec) | % Area |
|---|---|---|---|
| 1 | 2.16 | 113771 | 0.9 |
| 2 | 3.33 | 12409369 | 99.1 |

**Figure 2**. Chromatograms displaying racemic AZ11645373 (top) and pure fractions (fractions 1; $R_t$=2.25 min, and 2; $R_t$ = 3.33 min) from chiral separation.

Next, we wished to determine the absolute configuration of the separated enantiomers as this structural information was vital for establishing SAR and aiding in docking studies. Attempted crystallisation of either separated fraction was unsuccessful, yielding plates that did not diffract. However, palladacycles are known in the resolution of enantiomers and absolute structural determination [21]. In our case, given that the separated enantiomers were already available, we merely required the presence of the heavy metal complex to aid the crystallisation process. Formation of the pyridine-bound Pd complex **3** using fraction 2 was successful (scheme 1), on a small scale, and we were, gratifyingly, able to show that this fraction was the *(R)*-enantiomer (Figure 2) [22].

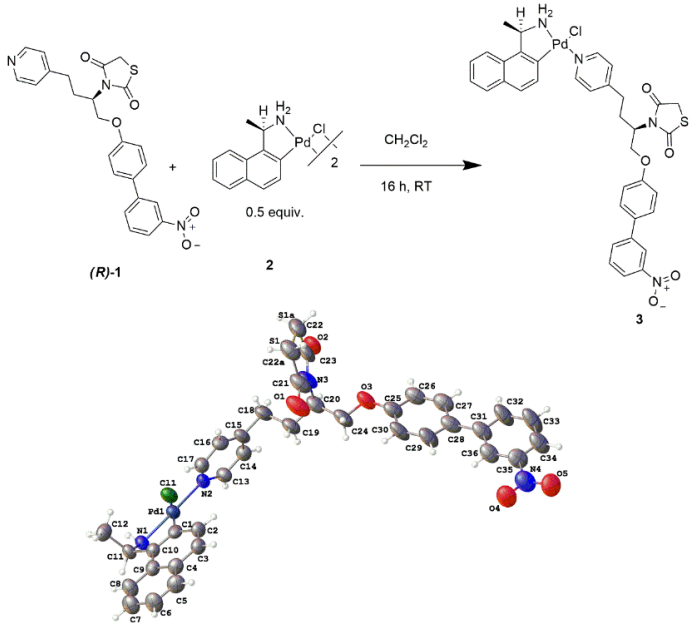


**Scheme 1**. Synthesis of a palladacycle complex of fraction 2, establishing its *(R)*-configuration.

The absolute configuration of the separated enantiomers was further, unambiguously, verified using VCD (Vibrational Circular Dichroism), a technique available for determination of stereochemical configuration of chiral molecules in the solution phase [23–26]. This was accomplished by the comparison of experimental IR and VCD spectra for each enantiomer to DFT calculated spectra of the *(R)*-configuration. The flexibility of this molecule resulted in over 300 conformers found in a 7 kcal/mol window molecular modelling search. These were subjected to optimization and frequency calculation at the 6-31G(d) / B3LYP DFT level. With

the relative energies obtained from this initial round of calculations, we carried on the lowest energy conformers through further rounds of DFT at different levels of theory to see which combination of basis set / functional would give the best results. The 60 lowest energy conformers were calculated at the 6-31G(d) / B3PW91 level, and the 30 lowest energy at both cc-pVTZ / B3LYP and cc-pVTZ / B3PW91 levels [27]. The smaller number of conformers was used with the large cc-pVTZ basis set due to the significantly longer calculation times. We obtained satisfactory results with all four methods, with the B3PW91 functional providing slightly better results overall than the B3LYP. The best match visually and statistically for the VCD spectra surprisingly came from the smaller 6-31G(d) basis set (Figure 3), while the larger cc-pVTZ basis set had a marginally better IR match. This may be due to the larger number of conformers calculated at the lower level. The calculated spectra had some minor frequency mismatches with the experimental; we suspect that the presence of the nitro group gave rise to some intermolecular and or solvent interactions which were not modelled in the DFT calculations. Fortunately, this did not prevent the confident assignment of absolute configuration for these compounds – all method results were analysed using BioTools (Jupiter, FL) CompareVOA software, with the 6-31G(d) / B3PW91 method having superior results. Neighbourhood similarity ($S_{fg}$) for both IR (80.1) and VCD (76.4) and confidence level (99) for the assignment were high, and the visual similarity, particularly for the VCD, was very good [28,29].

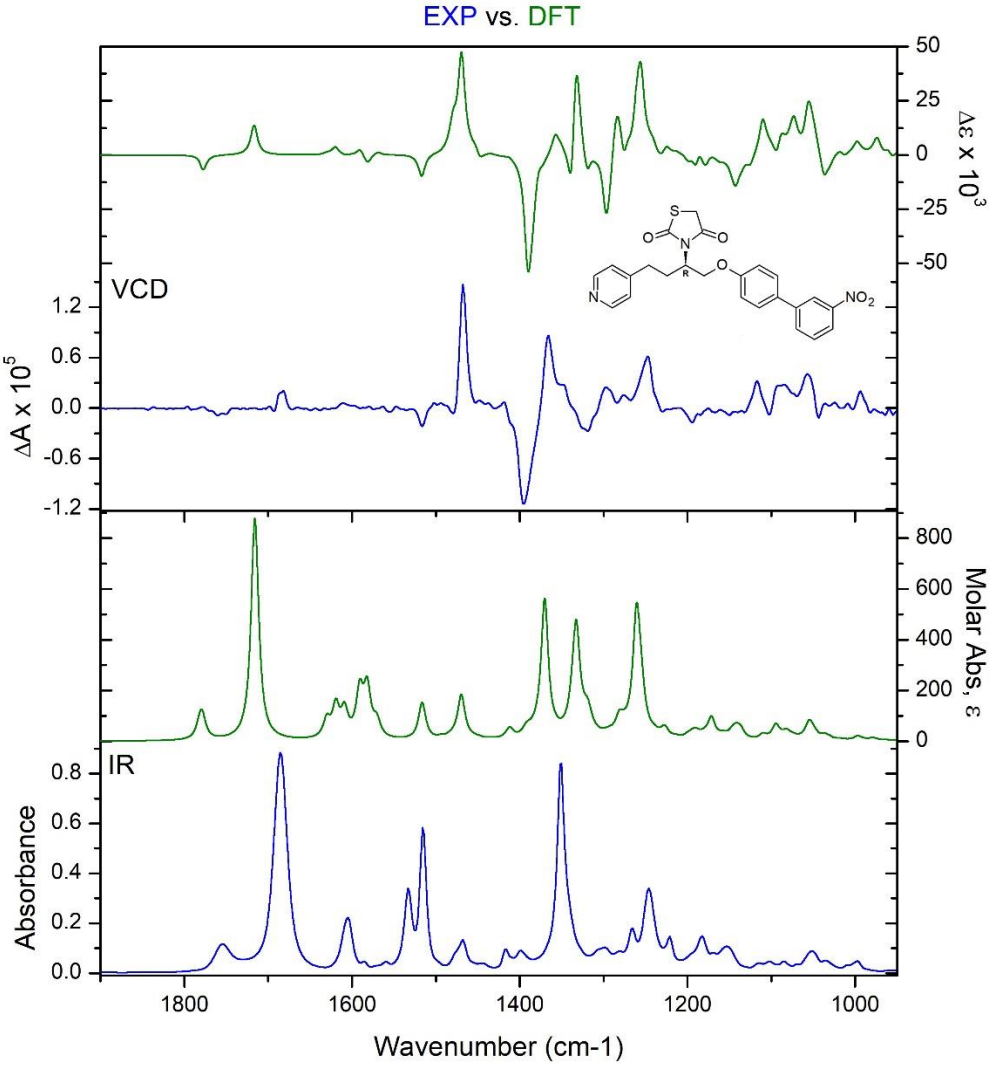


**Figure 3**. Determination of the *(R)*-configuration for **1**, fraction 2, using VCD.

The separation and the unequivocal determination of absolute configuration of both *(S)*- and *(R)*-enantiomers now paved the way for investigation of their biological functions. We used flow cytometry to simultaneously assess P2X7 calcium channel and large pore activities in HEK-293 cells expressing human P2X7 stained with the green calcium indicator Fluo-4 AM in the presence of the red DNA-binding dye TO-PRO-3, as previously described [30]. The synthetic P2X7 agonist BzATP induced a calcium influx and the opening of the large pore that resulted in the appearance of a cell population displaying Fluo-4 AM / TO-

PRO-3 double-positive staining (Figure 4). As expected, BzATP-induced Fluo-4 / TO-PRO-3 staining was inhibited by the racemic AZ11645373 (Figure 4A). *(S)*- and *(R)*- enantiomers also fully repressed calcium influx and large pore opening, demonstrating both enantiomers were antagonist to human P2X7.

We then carried out the same experiment on HEK-293 expressing mouse P2X7 (Figure 4B). Whereas the racemate efficiently repressed P2X7 functions, distinct results were obtained in the presence of the separated enantiomers. Contrary to its effect on human P2X7, *(S)*-AZ11645373 was ineffective on mouse P2X7, while its *(R)*-AZ11645373 enantiomer was a full antagonist. We then determined the half maximal inhibitory concentration ($IC_{50}$) of enantiomers on human and mouse P2X7 (Figure 4C). On human P2X7, both (*S*)- and (*R*)- forms were able to fully inhibit P2X7 but *(R)*-AZ11645373 was more potent, with an $IC_{50}$ of 32.9 nM, compared to its *(S)*-AZ11645373 ($IC_{50}$=1340 nM). On mouse P2X7, the *(S)*-enantiomer displayed a modest antagonistic activity at high concentrations, whereas *(R)*-AZ11645373 was efficient and slightly more potent than the racemate ($IC_{50}$=4940 nM). We also assessed the activity of the enantiomers on human P2X7-mediated early calcium influx using the calcium indicator Calbryte 520 AM staining, measured with a microplate reader (Supplementary Figure S2). As expected, we observed a rapid and sustained increase in intracellular calcium content in the presence of BzATP. This P2X7-mediated calcium influx was inhibited in the presence of *(R)*-AZ11645373 with an $IC_{50}$ of 66 nM, whereas *(S)*-AZ11645373 was less potent ($IC_{50}$=2675 nM), in accordance with later events evaluated by flow cytometry. Taken together, our results clearly show that *(R)*-AZ11645373 is the most potent enantiomer at P2X7 and is responsible for the antagonistic activity of the racemic AZ11645373.

Figure 4

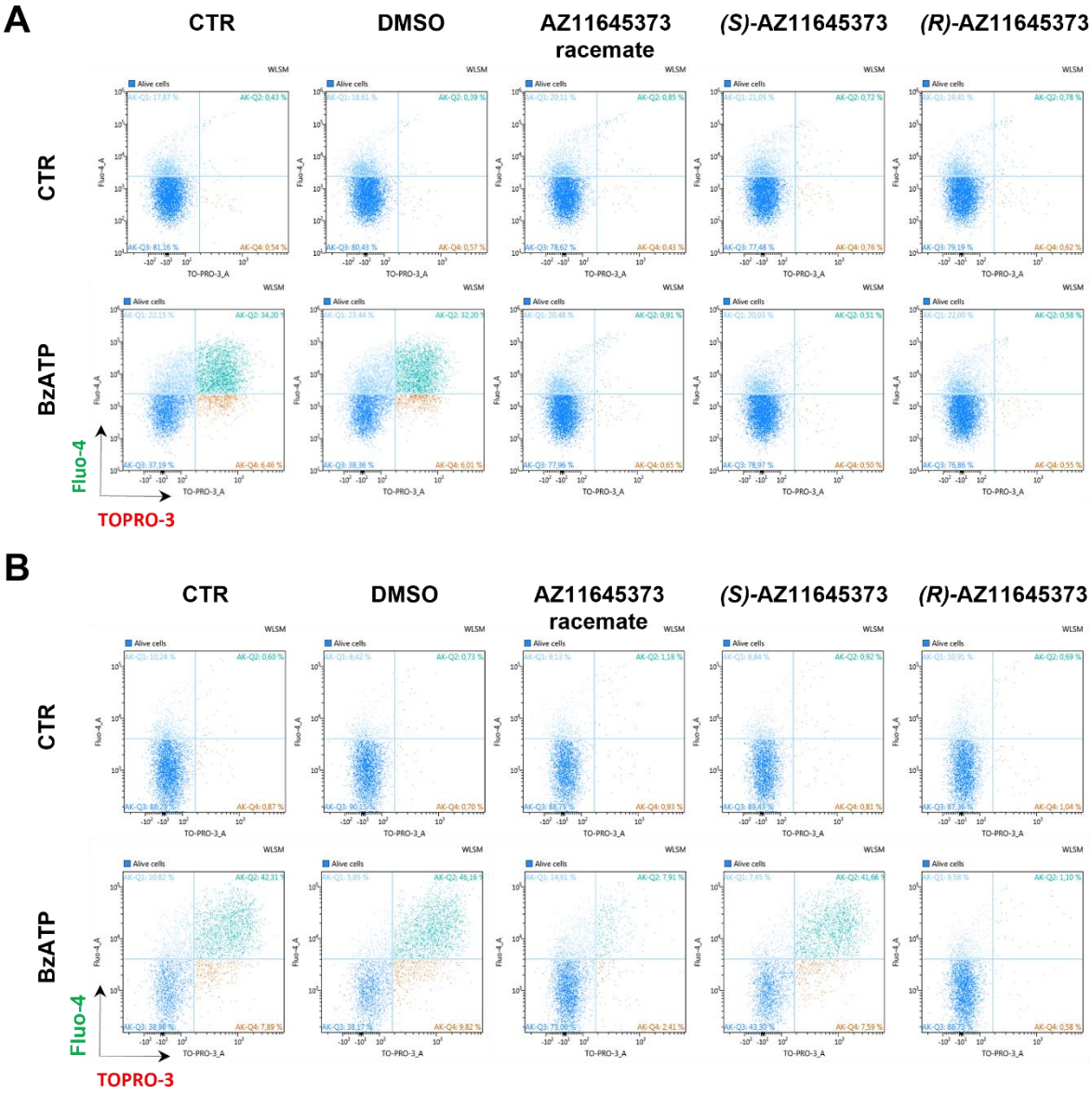

**Figure 4. Determination of AZ11645373 enantiomers' activity on P2X7.**

**A and B)** HEK-293 cells overexpressing human P2X7 **(A)** or mouse P2X7 **(B)** were stained with the calcium indicator Fluo-4 AM and then incubated with the non-permeant DNA-intercalating dyes TO-PRO-3 (large pore opening) and propidium iodide (cell viability) in the presence of indicated molecules at $10^{-5}$M for 15 min before addition of the P2X7 agonist BzATP (100 µM) for 30 minutes. The cells were then analysed by flow cytometry using SP6800 spectral cell analyser (Sony Biotechnology). Two-parameter plots of Fluo-4 AM *vs.* TO-PRO-3 fluorescence were done with SP6800 software. **C)** Percentages of Fluo-4 / TO-PRO-3 double-positive cells are plotted for calculation of half maximal inhibitory concentration ($IC_{50}$) of indicated compounds in HEK-293 cells overexpressing human (left panel) or mouse (right panel) P2X7. The results are representative of three independent experiments**.**

We then took advantage of the marked differences in efficacy of the enantiomers on mouse P2X7 to establish a competition between the enantiomers to compare their affinity for their binding site (Figure 5). The antagonist activity of the *(R)*-enantiomer, used at 10 µM, was only decreased by high concentrations of the *(S)*-enantiomer (100 µM), suggesting a greater affinity of compound *(R)* for the AZ11645373 binding site on mouse P2X7.

## Figure 5

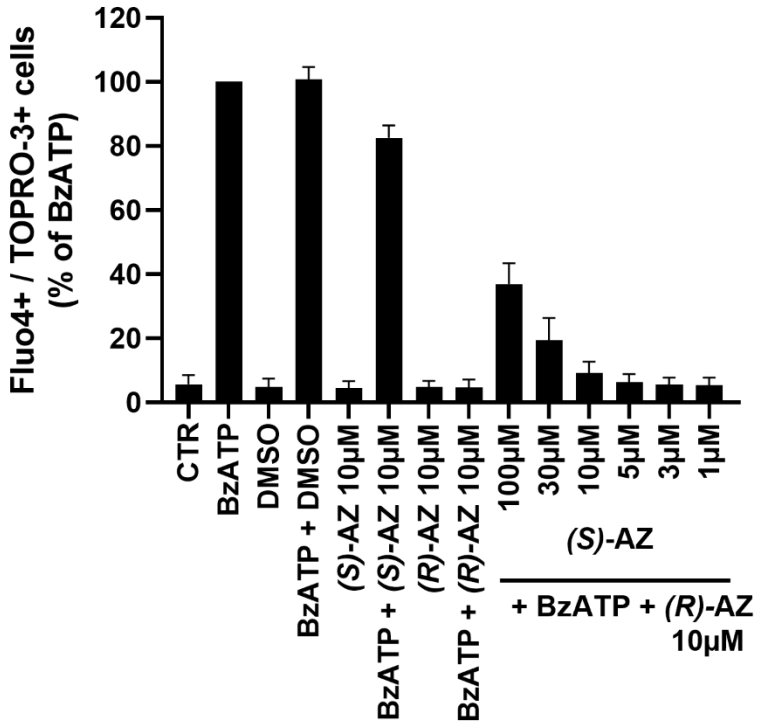


**Figure 5. Competition between AZ11645373 enantiomers for P2X7 binding.**

HEK-293 cells overexpressing mouse P2X7 were stained with the calcium indicator Fluo-4 AM and then incubated with the non-permeant DNA-intercalating dyes TO-PRO-3 (large pore opening) and propidium iodide (cell viability) in the presence of AZ11645373 enantiomers (*(S)*-AZ and/or *(R)*-AZ) at indicated concentrations for 15 min before addition of the P2X7 agonist BzATP (100 µM) for 30 minutes. The cells were then analysed by flow cytometry using SP6800 spectral cell analyser (Sony Biotechnology). Percentages of Fluo-4 / TO-PRO-3 double-positive cells are expressed as a percentage of maximal induction obtained with BzATP (100%). The results are representative of three independent experiments**.**

The crystallization of panda P2X7 in the presence of P2X7-selective antagonists has revealed an allosteric antagonist binding site, in a groove between two neighbouring subunits [13]. Crystallisation of P2X7 with AZ11645373 has not been performed but its binding to the allosteric binding site was determined with chimeras and point mutants [15]. The species-specific activity of AZ11645373, as a potent antagonist on human P2X7 but ineffective on rat P2X7, was explained by point mutations within the allosteric binding site, more precisely at V312, F108 and F95 (replaced by A312, Y108 and L95 in rat P2X7, respectively). Since mouse P2X7 also presents mutations compared to human P2X7 (A312 and Y108), we therefore verified whether these variant residues could explain the distinct antagonistic activity of AZ11645373 enantiomers in human and mouse P2X7 (Figure 6). Various mutants of mouse P2X7 were produced by site-directed mutagenesis, and stably transfected into HEK-293 cells. Amino acids at positions Y108 and A312 were substituted by their human counterparts: Y108F mutation, A312V mutation and a dual Y108F/A312V mutant as a mouse P2X7 with a "humanized" allosteric binding site. In the four different cell lines (expressing wild-type P2X7, Y108F, A312V, and the dual Y108F/A312V mutant), *(S)*- and *(R)*-AZ11645373 enantiomers were tested at different concentrations and P2X7 activity was evaluated by flow cytometry (Figure 6A). The double Y108F/A312V mutation enhances the potency of the compounds on mouse P2X7, which then exhibited efficacy similar to that in the human receptor (Figure 4C). Replacing alanine at position 312 with a valine also induced a marked improvement in potency, whereas a Y108F mutation had only a modest effect, indicating the interaction with V312 is relevant for both *(S)*- and *(R)*-enantiomers and mainly explains their species-specific activity.

Figure 6

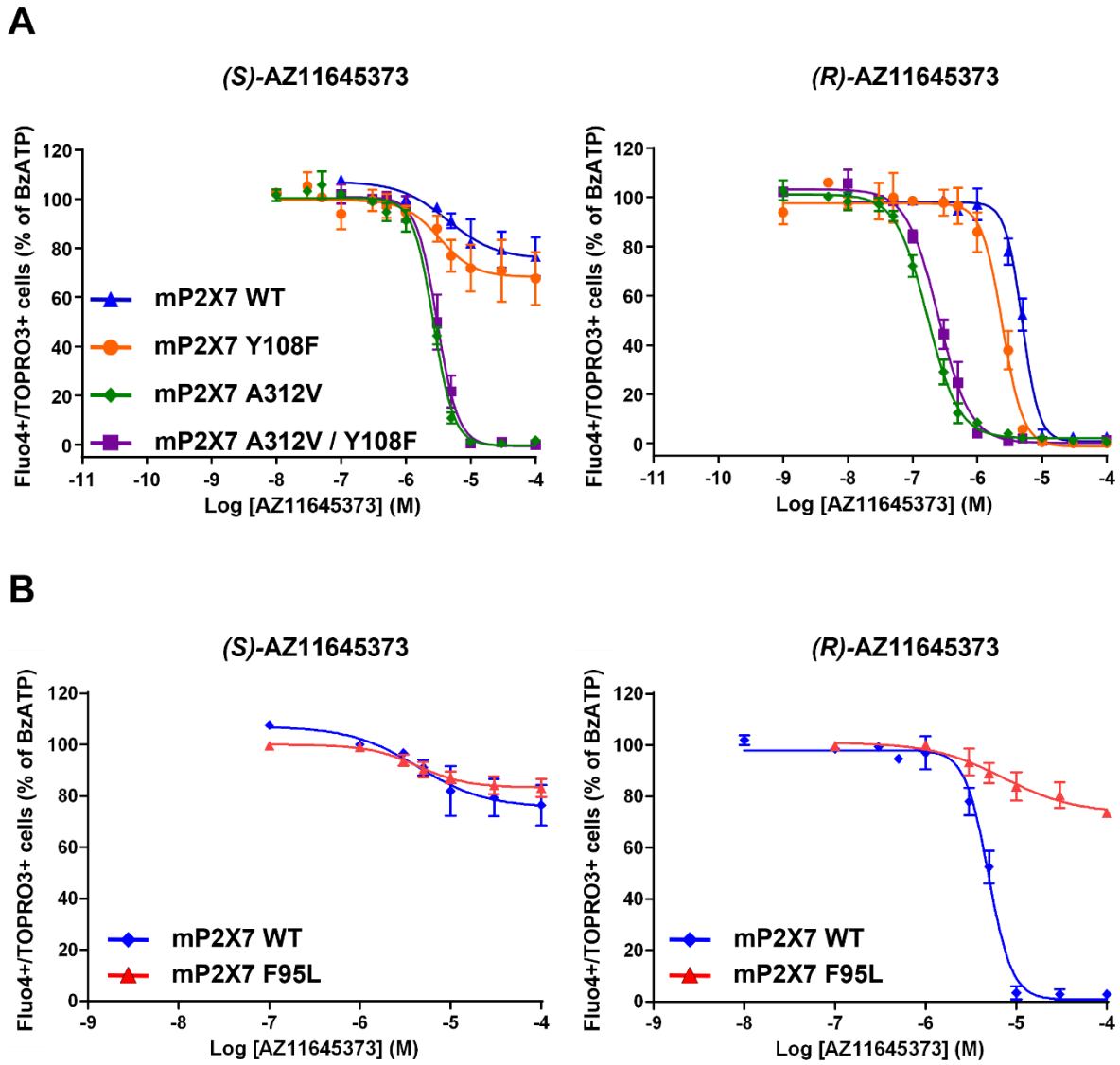


**Figure 6. Determination of AZ11645373 enantiomers' activity on mouse P2X7 mutants.**

HEK-293 cells overexpressing mutated mouse P2X7 were stained with the calcium indicator Fluo-4 AM and then incubated with the non-permeant DNA-intercalating dyes TO-PRO-3 (large pore opening) and propidium iodide (cell viability) in the presence of indicated molecules at $10^{-5}$M for 15 min before addition of the P2X7 agonist BzATP (100 µM) for 30 minutes. The cells were then analysed by flow cytometry using SP6800 spectral cell analyser (Sony Biotechnology). Percentages of Fluo-4 / TO-PRO-3 double-positive cells are plotted for calculation of half maximal inhibitory concentration ($IC_{50}$) of indicated compounds in HEK-293 cells overexpressing mouse P2X7 mutants: **A)**

mouse P2X7 wild-type (WT), Y108F, A312V and Y108F-A312V double mutant. **B)** mouse P2X7 wild-type (WT) and F95L. The results are representative of three independent experiments**.**

Another feature of racemic AZ11645373 is its lack of efficacy on rat P2X7 [15,17,19,20]. Rat P2X7 shares Y108 and A312 amino acids with mouse P2X7 but exhibits a leucine at position 95 instead of F95 on human and mouse counterparts. It was previously demonstrated that the F95L mutation abolished AZ11645373 efficiency on human P2X7, highlighting the essential role of F95 in racemic AZ11645373's activity [14,19,20]. We therefore substituted F95 by a leucine on mouse P2X7 and showed that F95L mutation strongly reduced the *(R)*-enantiomer's activity at a level similar to the *(S)*-enantiomer, whereas the latter's activity was unchanged, demonstrating that the effects of F95L mutation on racemic AZ11645373 are due to a loss of *(R)*-enantiomer efficacy. Compared to (*S*), the *(R)*-enantiomer might make specific interactions with F95 that can be essential in its species-selective activity.

### *In silico* insights into AZ11645373 P2X7 binding mode.

*In vitro* assays have demonstrated that AZ11645373 functions as a P2X7 modulator of the known allosteric binding site through site-directed mutagenesis [15]. The mouse and panda sequences exhibit 80% sequence identity and 85% identity within the allosteric region (Supplementary Figure S3). The structure of the pdP2X7 co-crystallised with the reference antagonist JNJ-47965567 (5U1X PDB entry [13]) was identified as the optimal template due to the shape similarity between JNJ-47965567 and AZ11645373, as illustrated by the bend formed by the oxane and thiazolidine chemical groups, respectively (Figure 1). The binding mode of the AZ11645373 enantiomers was identified by docking in the mouse P2X7 receptor model, which was created using homology modelling with pdP2X7-JNJ-47965567. Docking experiments of the reference JNJ-47965567 antagonist enabled the selection of the optimal docking protocol, which yielded the lowest

RMSD between the predicted JNJ-47965567 docking pose and the experimental co-crystallised JNJ-47965567 pose. In particular, the virtual binding sensitivity has been optimized by utilizing a search box encompassing the entire extracellular region and selecting the most favorable docking pose by the *Vina* score . All the preliminary docking studies of the co-crystallised reference compounds have shown that two allosteric binding sites should be occupied in order that the predicted docking solution could be correlated to the experimental pose into the vacant site. That is why the docking of AZ11645373 has been performed in only one vacant allosteric site (chain C) whereas the two other sites (chains A and B) were occupied by JNJ-47965567. The docking protocol indicates that both the *(S)*- and *(R)*- enantiomers of AZ11645373 are capable of fitting into the allosteric binding site of chain C (chains A and B kept bound to JNJ-47965567), adopting conformations that are superimposed on the bent shape of JNJ-47965567 (Figure 7). Therefore, in one instance, *(R)*-AZ11645373 displays a pyridyl group orientated towards the pore channel, analogous to the positioning of JNJ-47965567's phenyl group. This results in the formation of an aromatic interaction with Phe95. In contrast, (*S*)-AZ11645373 presents the thiazolidine group in proximity to Phe95, thereby disrupting the aromatic interaction observed with JNJ-47965567, *(R)*-AZ11645373, and other co-crystallized compounds, including allosteric antagonists such as A-740003 and GW791343 [13]. It is noteworthy that Phe95 is identified as a pivotal residue for P2X7 modulation by racemic AZ11645373 in human P2X7 [15]. Furthermore, the same phenomenon occurs in rat P2X7 [31], where position 95 is a non-aromatic leucine residue, rendering AZ11645373 inactive. Furthermore, the three-dimensional analysis of the P2X7-JNJ-47965567 channel reveals the presence of an aromatic lock between the Phe95 residues of each monomer, which modulates an aromatic lock of the upper channel in conjunction with the JNJ-47965567 allosteric ligands (Figure 8). The close resemblance in the arrangement of aromatic substituents and shape between JNJ-47965567 and *(R)*-AZ11645373 coupled with the conservation of Phe95 between the panda experimental and mouse model structures, lends considerable support to the likelihood of this intermolecular prediction. To gain further insight into the stability of the homotrimeric mouseP2X7-*(R)*-AZ11645373 (C), JNJ-47965567 (A,B) and mP2X7-*(S)*-AZ11645373 (C), JNJ-47965567 (A,B) complexes embedded in a membrane, triplicated 200 ns molecular dynamics (MD) simulations have been conducted

(see Electronic supplementary materials). This approach permits a more comprehensive investigation of the intermolecular interactions within the complexes. The stability of *(R)*-AZ11645373 within the allosteric binding site is markedly greater than that of *(S)*-AZ11645373 at the entropy level. The maximal RMSD is 3.5 Å, while the average RMSD is 2.75 Å in the case of *(R)*-AZ11645373, in comparison to *(S)*-AZ11645373, which displays an RMSD of at least twice that value (7.2 Å) with an average RMSD of 5.8 Å (Figure 9A). From an enthalpy perspective, the analysis of intermolecular contacts indicates that an ionic interaction between the nitro group of *(R)*-AZ11645373, Glu305(A) and Lys297(C) or Lys110(C) is likely to be maintained (Figure 9B + Supplementary Figure S4). This is not the case for *(S)*-AZ11645373 across all three simulations (Figure 9B + Supplementary Figure S4). At the opposite end of the antagonist, the pyridine group of *(R)*-AZ11645373 is almost continually maintained within an aromatic cage formed by Phe95(C), Tyr295(C) and the terminal pyridine group of JNJ-47965567(A) throughout the MD simulations. While these contacts are also observed between these amino acids and *(S)*-AZ11645373, they are not frequent aromatic contacts but rather van der Waals (VdW) contacts (Supplementary Figure S4). It is noteworthy that only *(R)*-AZ11645373 is observed to interact significantly by aromatic contacts that differ from those of its host chain (chain C), particularly with Tyr298(A) and JNJ-47965567(A).

**Figure 7. Docking of AZ11645373 racemic into JNJ-47965567 -templated mP2X7 model.**

*(R)*-AZ11645373 and *(S)*-AZ11645373 are illustrated in beige and cyan respectively whereas the co-crystallised pose of JNJ-47965567 (5U1X.pdb) appears in green.

**Figure 8. Phe95 aromatic lock**.

**(A)** Extracellular view of crystal homotrimeric *pd*P2X7 structures depicting superimposition of allosteric antagonists in interaction with the three Phe95 residues represented as ball and stick: JNJ-47965567 (green), AZ10606120 (pink) and A804598 (blue). **(B)** Pore surface of pdP2X7-JNJ-47965567 channel as represented from ChannelDB 2.0 webserver [32].

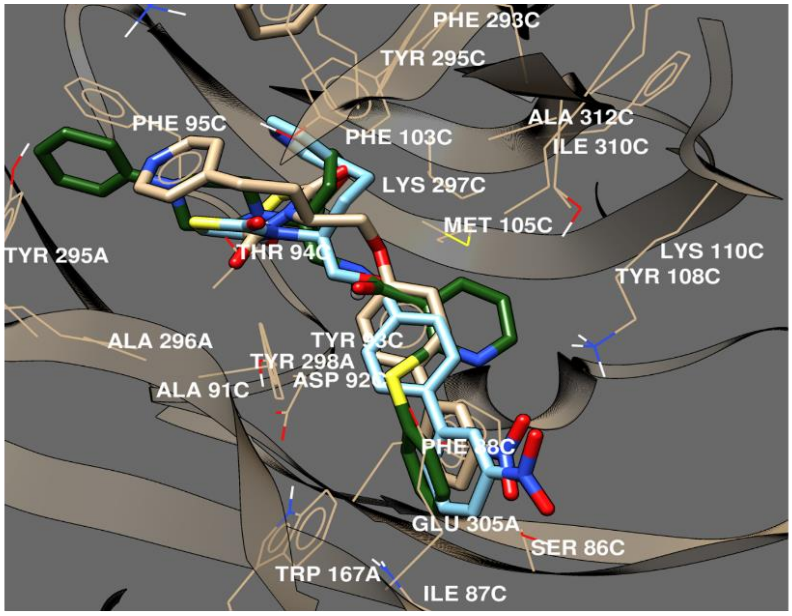


**Figure 7**

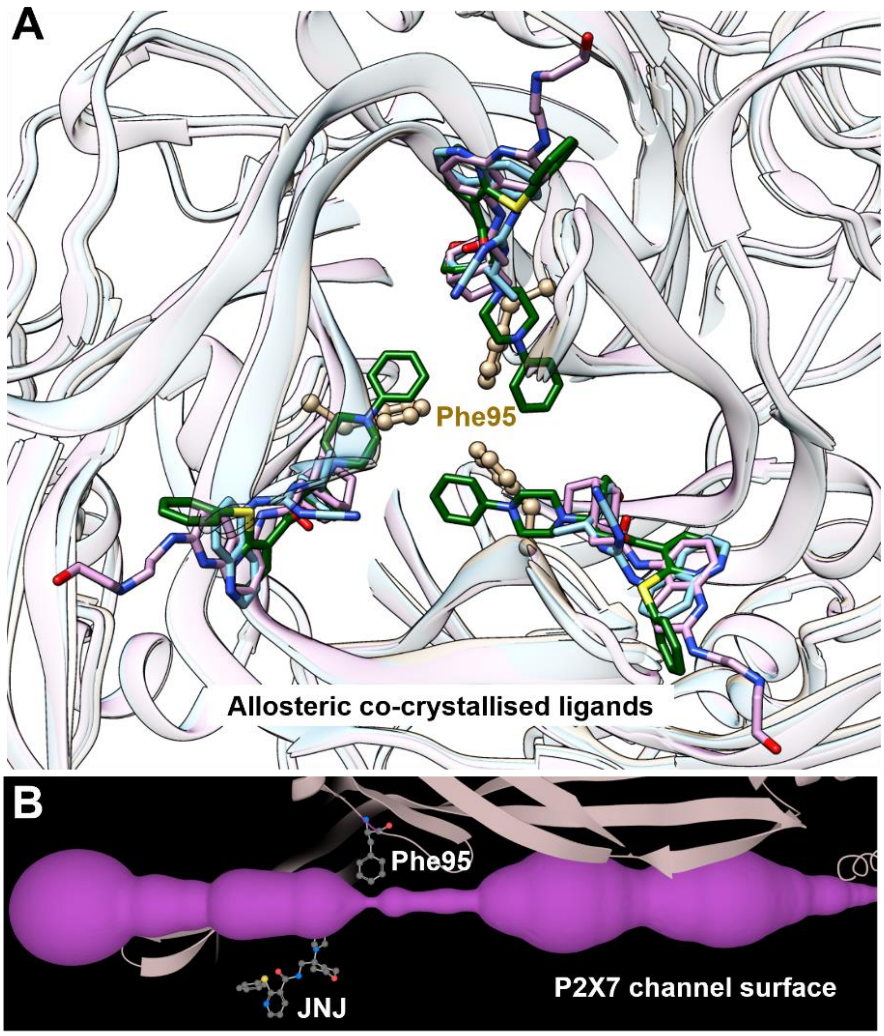


**Figure 8**

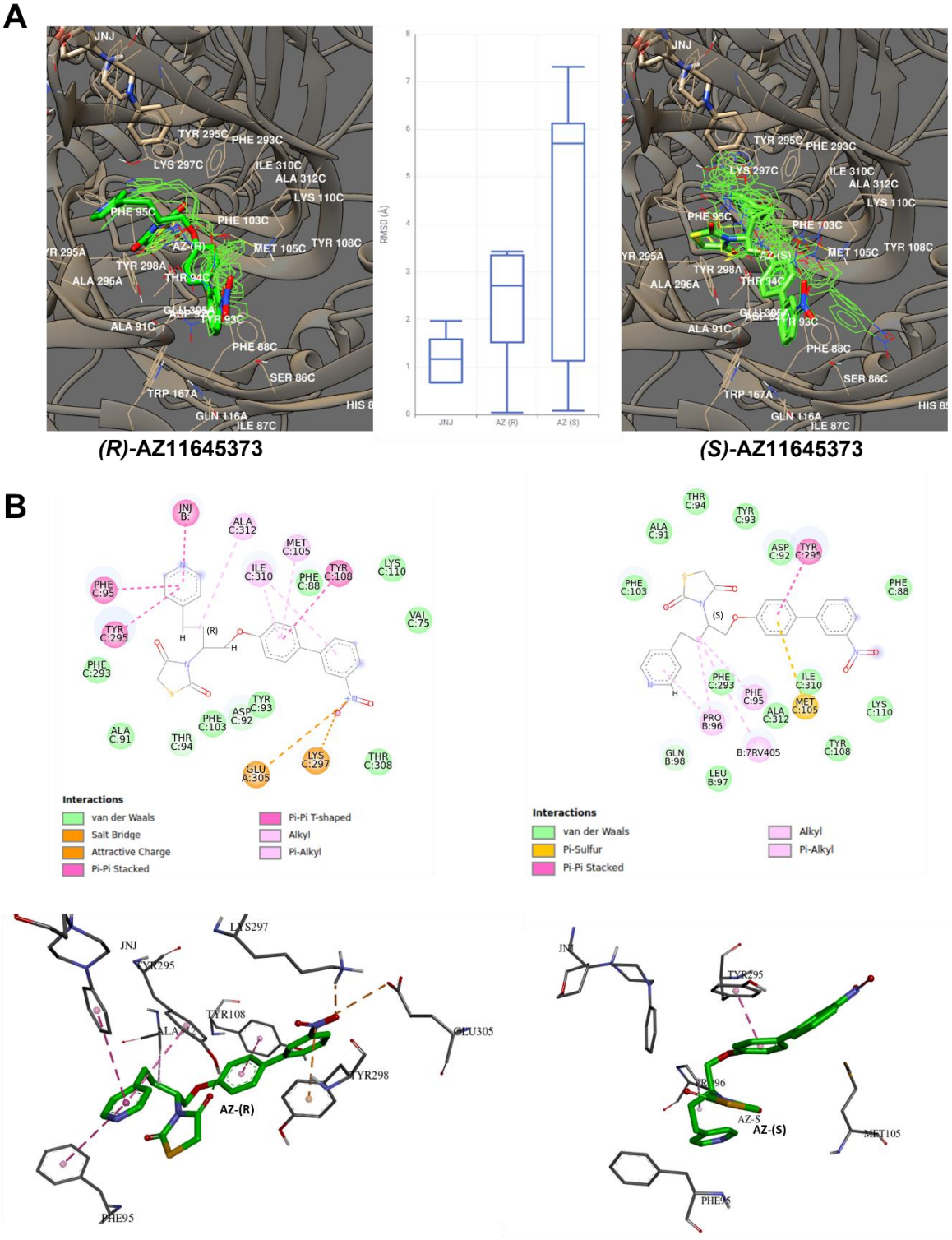


**Figure 9**

**Figure 9. MD-derived mP2X7-AZ11645373 intermolecular spots.**

**(A)** Structural deviation of representative AZ11645373 conformers isolated from triplicated 200ns MD simulations of both mP2X7-*(R)*-AZ11645373 and mP2X7-*(S)*-AZ11645373 complexes at 3D (left and right panel with AZ11645373 compounds in green and initial pose in stick) and analytics (box plot displaying RMSD dispersion between MD conformers) levels. **(B)** Intermolecular interactions from one 200 ns MD simulation for each complex (supporting information).

This study adds weight to the argument for the use of single enantiomers to enhance biological properties and reduce side effects and toxicity, e..g cytotoxicity, which can halt a drug in preclinical studies [33]. We measured the potential cytotoxic effect of our pure enantiomers in cell proliferation assays (Figure 10). The racemic AZ11645373 induces a 60% decrease in proliferation of HEK-293 expressing human or mouse P2X7 but also in untransfected cells, demonstrating this cytotoxic effect is not related to P2X7 expression. The separation of the enantiomers does not improve this off-target effect since both *(S)*- and *(R)*-enantiomers affect cell proliferation in a similar manner. However, these cytotoxic effects are no longer observed at 1 µM, a concentration at which the *(R)*-enantiomer is still active at the human receptor. The *(R)*-enantiomer may then be a beneficial alternative to the racemic mixture to increase antagonist potency and to remove the *(S)*-enantiomer's competition for binding site and its potential adverse cytotoxic activity.

Figure 10

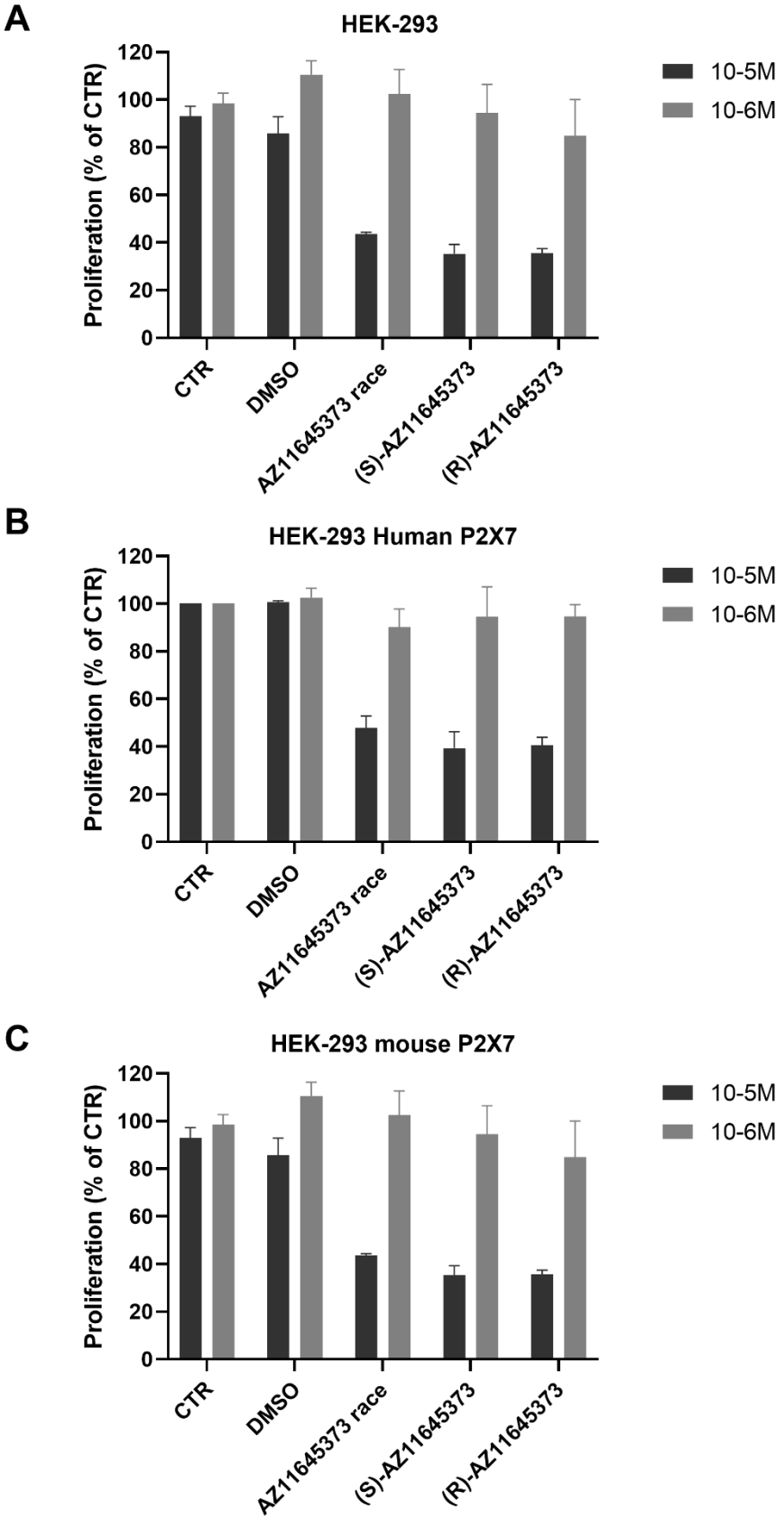

**Figure 10. Cytotoxicity induced by AZ1164537311 enantiomers.**

HEK-293 cells **(A)** or HEK-293 cells overexpressing human P2X7 **(B)** and mouse P2X7 **(C)** were treated with indicated concentrations of AZ11645373 racemic mixture or *(S)*- and *(R)*-enantiomers. Cell proliferation was measured after 72 hours. Results are expressed as percentage of proliferation compared to control cells. The results are representative of three independent experiments**.**

## CONCLUSION

The separation of AZ11645373 enantiomers and subsequent biological evaluation have been useful to precise structure-activity relationships of the molecules and for determining molecular mechanism of P2X7 antagonism. With regard to the structure-function relationships, the P2X7 receptor presents a particularly intriguing case, given the intricate structural complexity. This encompasses two distinct isoform structures (P2X7A and P2X7B) [5], a paucity of data regarding intermediate metastable states including potentially other allosteric binding sites, the macropore enigma [8] and noteworthy interspecies contrasted structure-activity relationships [13,20]. The study of the stereoselectivity of this reference allosteric antagonist enabled us to identify minor chemical modifications with a significant impact on pharmacological activity. In the context of the multi-factorial structure-activity relationships identified above, this study enables us to focus solely on the following aspects: (i) the allosteric site, previously demonstrated to be the binding site for AZ11645373; (ii) the closed state, with multiple PDB structures co-crystallised with reference allosteric antagonists; and (iii) the highly homologous mouse species (80% compared to panda sequence), the most relevant experimental model for pre-clinical studies of drug candidates. Nevertheless, the results were only obtained from the truncated isoform [13], devoid of the cytoplasmic domain, admitting that the dynamics of

intermolecular interactions into the allosteric site would not be affected in the context of the full-length sequence.

The combination of i*n silico* results emphasises the differential binding profile between the two enantiomers, with *(R)*-AZ11645373 displaying the greatest stability in the allosteric binding site and exhibiting the most significant aromatic contacts between the three aromatic cycles and amino acids known to be critical for AZ11645373 activity (Phe88, Phe95, Tyr108, Tyr295). In light of the preceding *in silico* P2X7-AZ11645373 intermolecular study [15], which posited the stereospecificity of the *(S)*-AZ11645373 enantiomer, we concur that docking was inadequate for discriminating between the binding modes of both enantiomers. To gain further insight, it is beneficial to couple this approach with other techniques, such as molecular dynamics simulations, to identify the specific intermolecular interactions that contribute to the high stability of *(R)*-AZ11645373 within a monomer, primarily through aromatic contacts. Furthermore, *(R)*-AZ11645373 exhibits a proclivity for orienting itself in a manner that enables it to interact with one of the two other allosteric ligands, namely JNJ-47965567, through aromatic contact. This observation lends support to the hypothesis that the allosteric function of *(R)*-AZ11645373 may be attributed to a cooperative aromatic binding network between the three allosteric inhibitors and the three Phe95 residues. As demonstrated by the research of Stokes *et al*. [17], AZ11645373 has been proven to be 500 times more active for the human than for the rat P2X7 receptor, which features a leucine amino acid in position 95 instead of aromatic phenylalanine in the mouse, human, and panda sequences (Supplementary Figure S3). In the light of this observation and our results, Phe95 is located at the boundary between the channel pore and the allosteric site and appears to be the pivotal molecular gateway between AZ11645373 allosteric binding and locking of the closed state of the P2X7 channel. These key receptor-ligand interactions are relevant to explain the efficiency of the antagonists with a binding mode similar to *(R)*-AZ11645373 and have to be taken into account for the future rational design of new potent compounds.

## METHODS

### Cell culture

HEK-293 cells stably expressing human or mouse P2X7 were established as described [30]. The cells were cultured in DMEM medium with Glutamax (Life Technologies), supplemented with 10% heat-inactivated foetal calf serum, 1000 UI/mL penicillin, 1000 µg/mL streptomycin and incubated at 37°C in 5% $CO_2$. Stable cell lines were grown in medium supplemented with 5 µg/mL blasticidin (Sigma-Aldrich) to select P2X7-overexpressing cells.

### Site-directed mutagenesis and generation of cell lines

The pcDNA6-mouse P2X7 plasmid was a kind gift from Dr Valerie Vouret-Craviari (University of Nice, France). Plasmids expressing mouse P2X7 mutants were obtained by site-directed mutagenesis using In-Fusion® HD cloning kit (Takara), according to manufacturer's instructions. The presence of the correct mutations and absence of undesired mutations were checked by whole plasmid sequencing (Eurofins Genomics). Plasmids were transfected into HEK-293 using Lipofectamine 3000 (Life Technologies), according to manufacturer's instructions. Stably transfected cells were selected with blasticidin resistance and stable cell lines were sorted according to P2X7 membrane expression using anti-mouse P2X7 antibody (1F11, BioLegends), using SH800 cell sorter (Sony Biotechnology).

### Flow cytometry

P2X7-induced increase in intracellular calcium concentration and plasma membrane permeabilization (large pore opening) were assessed by flow cytometry analysis using, respectively, Fluo-4-AM fluorescent dye and the membrane impermeant DNA-intercalating dye TO-PRO-3 (Life Technologies), as described

previously [30]. Briefly, the cells ($10^6$ cells / mL) were loaded with Fluo-4 AM (50 nM) for 30 min in culture medium without foetal calf serum at 37°C. The cells were then centrifuged at 230 g for 5 min and resuspended in sucrose buffer (20 mM HEPES, 300 mM sucrose, 5 mM KCl, 1 mM $MgCl_2$, 1 mM $CaCl_2$, 10 mM glucose, pH 7.4) containing TO-PRO-3 (10 nM) and propidium iodide (75 nM). The cells ($10^5$ in 200 µL) were treated with BzATP and/or different compounds for 30 min at room temperature and analysed by SP6800 spectral cell analyser (Sony Biotechnology) using SP6800 software. Highly PI-positive cells were considered as dead cells, strongly stained by TO-PRO-3 due to disrupted plasma membrane (i.e. independently of P2X7 activation) and were gated out using SP6800 software [30].

**Calcium influx measurements**

HEK-293 cells overexpressing human P2X7 were harvested and 30.000 cells per well were seeded on a poly-L-Lysine-coated 96 well plate in complete medium. Twenty four hours later, cells were washed with culture medium without foetal calf serum and loaded with the calcium indicator Calbryte 520 AM (1 µM) for 1 hour in culture medium without foetal calf serum at 37 °C. The cells were then washed and resuspended in sucrose buffer (20 mM HEPES, 300 mM sucrose, 5 mM KCl, 1 mM $MgCl_2$, 1 mM $CaCl_2$, 10 mM glucose, pH 7.4) for 30 minutes. Sucrose buffer was then removed and tested compounds at $10^{-5}$M were added in sucrose buffer for 15 minutes. Calbryte fluorescence intensity was measured with a Clariostar Plus (BMG Labtech), with a 490 nm excitation wavelength and an emission at 530 nm. BzATP was injected (100µM final) after 3 seconds of baseline measurement and fluorescence intensities were measured during 35 seconds.

**Cell Proliferation Assay.**

HEK-293 cells overexpressing human P2X7 (3000 cells/well) were seeded in triplicates on 96 well plates in 100 µL culture medium and incubated for 24 h. Cells were then treated with tested compounds. After 72 h, cell growth was measured using the CellTiter 96® Aqueous One Solution Cell Proliferation Assay (Promega, Madison/WI, USA), in accordance with the manufacturer's instructions. The results are expressed as percentage of proliferation compared to control cells.

**Models of the P2X7 structure.**

Murine P2X7 receptor models have been constructed using the Modeller program [34] through homology with the pdP2X7 (5U1X PDB entry [13]) structure that was co-crystallised with JNJ-47965567. The coordinates of JNJ-47965567 have been incorporated into the homotrimeric P2X7 model, which was then subjected to geometry refinement of the side chains and the three ligands via energy minimisation until a 0.001 RMS gradient was achieved with the AMBER14 force field.

**Docking experiments.**

Blind docking has been performed removing the JNJ-47965567 ligand of chain C using the Gnina docking engine [35] with searching exhaustiveness set up at 64, 128 or 256 Dkoes, Vina or Vinardo scoring functions, the default CNN rescoring, the CrossDock-2018 ensemble and a searching box that included either the entire mP2X7 receptor model or only the extracellular region.

**Molecular Dynamics simulations.**

Molecular dynamics simulations of mP2X7-*(S)*-AZ11645373 and mP2X7-*(R)*-AZ11645373 were conducted in triplicate over 200 ns computed periods at 298K in NPT ensemble using the standard parameters of the AMBER14 force field through YASARA 23.12.24 [36]. The *md_runmembrane* script of YASARA first centered the complex model into a cuboid box and scanned this solute in order to predict and orient the protein helix elements to be embedded into a membrane lipid bilayer of POPC (1-palmitoy-2-oleyl phosphatidylcholine). Following replication of the POPC samples to fit the dimensions of the

protein and membrane compression to reach a total lipid head area of 100 x 100 $A^2$, each mP2X7-AZ11645373 complex was embedded and solvated with water and NaCl 0.9%. Subsequently, the systems underwent several cycles of steepest descent and simulated annealing minimization to remove irregularities in the membrane following the deletion of water molecules. Following 250 ps of equilibration, position restraints were released for trajectory production up to 200 ns, allowing the protein backbone and ligand positions to move freely.

**AZ11645373**. This was purchased from eNovation (https://www.enovationchem.com) and used as such, separated (see ESI) at Reach Separations into respective fractions 1 ((*S*)-) and 2 ((*R*)-) enantiomers. $^1$H NMR (600 MHz, DMSO-$d_6$) δ 8.46 – 8.42 (m, 2H), 8.36 (t, *J* = 2 Hz, 1H), 8.14 (dd, *J* = 8, 2 Hz, 1H), 8.08 (dt, *J* = 8, 1 Hz, 1H), 7.73 – 7.67 (m, 3H), 7.23 – 7.19 (m, 2H), 7.04 – 6.98 (m, 2H), 4.53 (m, 1H), 4.45 (t, *J* = 10 Hz, 1H), 4.29 (dd, *J* = 10, 5 Hz, 1H), 4.17 (d, *J* = 3 Hz, 2H), 2.63 (t, *J* = 8 Hz, 2H), 2.32 – 2.30 (m, 1H), 2.11-2.09 (m, 1H).$^{13}$C NMR (151 MHz, DMSO-$d_6$) δ 173.0, 178.9, 158.8 (2C), 150.2, 150.2, 148.9, 141.7, 133.2, 131.0, 130.9, 128.7, 124.2, 120.9, 115.8, 66.6, 53.9, 33.8, 31.2, 27.9.
Mass spectrum; $C_{24}H_{21}N_3O_5S$ Calculated [M+H] = 464.1280. Experimental [M+H] = 464.1275 (ppm = 0.2) (Supplementary Figure S5). Purity on HPLC from Reach Separations was over 95%.

Synthesis of (*R*)-**3**. Compound **2** dimer (36 mg, 0.5 eq) and AZ11645373 ((*R*)-, fraction 2) (50 mg, 1.0 eq) were dissolved in anhydrous $CH_2Cl_2$ (DCM) and stirred at room temperature for 16 hours. Upon completion the reaction mixture was concentrated to dryness and purified by column chromatography ($SiO_2$, 4 g, DCM:MeOH 95:5 to 80:20 over 14 minutes). Compound **3** was isolated as a pale-yellow solid (60 mg, 70%) from which a few x-ray quality crystals were grown using vapour diffusion over 72 hours (DCM and hexanes). $^1$H NMR (600 MHz, Chloroform-*d*) δ 8.75 (d, *J* = 6 Hz, 2H), 8.37 (s, 1H), 8.14 (d, *J* = 8 Hz, 1H), 7.84 (d, *J* = 8 Hz, 1H), 7.56 (t, *J* = 8 Hz, 1H), 7.53 (d, *J* = 8 Hz, 2H), 7.20 (d, *J* = 6 Hz, 2H), 7.01 – 6.95 (m, 2H), 6.95 (s, 1H), 6.90 (d, *J* = 7 Hz, 1H), 6.75 (t, *J* = 7 Hz, 1H), 6.01 (d, *J* = 8 Hz, 1H), 4.74 (q, *J* = 8 Hz, 1H), 4.48 (t, *J* = 8 Hz, 1H), 4.24 – 4.19 (m, 1H), 3.92 – 3.83 (m, 3H), 2.93 – 2.83 (m, 2H), 2.74 (s, 3H),

2.66 (s, 2H), 2.63 (s, 1H), 2.16 (m, 1H), 1.66 (s, 1H), 1.57 (d, *J* = 7 Hz, 1H). m/z. negative ion mode; Experimental Mass [M-H] 773.0822; Calcd; [M-H] 773.0817 for $C_{36}H_{32}N_4O_5SClPd$

**VCD Measurements**: A 100uL solution containing 4.2 mg of chiral nitro compound dissolved in $CDCl_3$ was transferred to a $BaF_2$ IR cell with path length of 100 µm. Instrumentation was a BioTools (Jupiter, Florida) ChiralIR 2X DualPEM FT-VCD, resolution 4 $cm^{-1}$, PEM maximum frequency 1400 $cm^{-1}$. The samples were measured for 12 blocks of 1 hour each while purged with dry air to remove water vapor. The IR was processed by solvent subtraction and offset to zero at 2000$cm^{-1}$. The VCD blocks were averaged, then baseline corrected using the opposite enantiomer measured at the same concentration (then divided by 2) to produce the final spectrum.

**VCD Calculations**: Chiral nitro compound (*R*-configuration) was subjected to a conformer search (GMMX, MMF94) search using BioTools ComputeVOA software to find the lowest energy conformers in an 7 kcal/mol range (311 total). All conformers were minimized using Gaussian 09 at the 6-31G(d) / B3LYP level with CPCM solvent (chloroform) model. IR and VCD frequencies were calculated at the same level, then duplicates were removed. The lowest energy unique conformers were then re-calculated at the cc-pVTZ / B3LYP and cc-pVTZ / B3PW91 (30 conformers each) level and the 6-31G(d) / B3PW91 (60 conformers) level, and the resulting spectra from all four methods were Boltzmann averaged and plotted with a line width of 5 $cm^{-1}$. IR and VCD spectra were then frequency scaled (uniform factor of 0.96 to 0.98 depending on functional and basis set) and compared to the experimental data.

**Acknowledgements**. This work was funded by the Strategic Development Fund and HEIF Covid Emergency Funds (University of Sussex), Institut National de la Santé et de la Recherche Médicale (INSERM) and the University of Lille**.** Dr Paul Kemmit (AZ, Cambridge) is thanked for helpful discussions. We thank Nathalie Jouy, Emilie Floquet from Bio Imaging Center Lille Nord-de-France Flow Cytometry Core Facility, Maria Michalak, Morgane Breuninger, Romane Raison and Charles Paul-Constant for technical assistance.

**Author contributions**.

A. M., N. R., A. B., J. N., L. B., D. G., G. J. T., S. J. C., D. L., D. v E., L. S., K. B., L. E., B. W. G., R. M., J. S., X. D. performed the experiments and analysed the data.

A. M., N. R., J. S., X. D. wrote the manuscript.

N.R., J.S. and X.D. supervised the project.

**Supporting information.**

**Supplementary Figure S1: Chiral integrity, two years after initial chiral separation.**

**Supplementary Figure S2: Measurement of P2X7-mediated calcium influx in the presence of AZ11645373 enantiomers.**

HEK-293 cells overexpressing human P2X7 were stained with the calcium indicator Calbryte 520 AM and incubated in the presence of AZ11645373 enantiomers at indicated concentrations (nM) before addition of the P2X7 agonist BzATP. Fluorescence was measured in triplicates with the microplate reader Clariostar Plus. BzATP was injected (100µM final) after 3 seconds of baseline measurement and fluorescence intensities were measured during 35 seconds. Control cells (CTR) were left untreated. The results are representative of three independent experiments.

**Supplementary Figure S3: Multiple sequence alignment of mouse, rat, Human and panda P2X7 sequences.**

**Supplementary Figure S4: mouseP2X7-AZ11645373 binding occurencies during Molecular Dynamics.**

Intermolecular contacts are depicted for triplicate of mP2X7-*(R)*-AZ11645373 and mP2X7-*(S)*-AZ11645737 such as hydrogen bonds (HB), hydrophobic (Hyd), ionic (Ion) or hybrid interactions.

**Supplementary Figure S5: HRMS of AZ11645373.**

**Electronic Supplementary Materials: Trajectory files of Molecular Dynamics simulations**

## REFERENCES


(1) Burnstock, G.; Knight, G. E. The Potential of P2X7 Receptors as a Therapeutic Target, Including Inflammation and Tumour Progression. *Purinergic Signal.* **2018**, *14* (1), 1–18. https://doi.org/10.1007/s11302-017-9593-0.

(2) Burnstock, G. Purine and Purinergic Receptors. *Brain Neurosci. Adv.* **2018**, *2*, 2398212818817494. https://doi.org/10.1177/2398212818817494.

(3) Andrejew, R.; Oliveira-Giacomelli, Á.; Ribeiro, D. E.; Glaser, T.; Arnaud-Sampaio, V. F.; Lameu, C.; Ulrich, H. The P2X7 Receptor: Central Hub of Brain Diseases. *Front. Mol. Neurosci.* **2020**, *13*, 124. https://doi.org/10.3389/fnmol.2020.00124.

(4) Adinolfi, E.; Giuliani, A. L.; De Marchi, E.; Pegoraro, A.; Orioli, E.; Di Virgilio, F. The P2X7 Receptor: A Main Player in Inflammation. *Biochem. Pharmacol.* **2018**, *151*, 234–244. https://doi.org/10.1016/j.bcp.2017.12.021.

(5) Di Virgilio, F.; Dal Ben, D.; Sarti, A. C.; Giuliani, A. L.; Falzoni, S. The P2X7 Receptor in Infection and Inflammation. *Immunity* **2017**, *47* (1), 15–31. https://doi.org/10.1016/j.immuni.2017.06.020.

(6) Young, C. N. J.; Górecki, D. C. P2RX7 Purinoceptor as a Therapeutic Target—The Second Coming? *Front. Chem.* **2018**, *6*. https://doi.org/10.3389/fchem.2018.00248.

(7) Di Virgilio, F.; Schmalzing, G.; Markwardt, F. The Elusive P2X7 Macropore. *Trends Cell Biol.* **2018**, *28* (5), 392–404. https://doi.org/10.1016/j.tcb.2018.01.005.

(8) Peverini, L.; Beudez, J.; Dunning, K.; Chataigneau, T.; Grutter, T. New Insights Into Permeation of Large Cations Through ATP-Gated P2X Receptors. *Front. Mol. Neurosci.* **2018**, *11*, 265. https://doi.org/10.3389/fnmol.2018.00265.

(9) Mishra, A.; Behura, A.; Kumar, A.; Naik, L.; Swain, A.; Das, M.; Sarangi, S. S.; Dokania, P.; Dirisala, V. R.; Bhutia, S. K.; Mishra, A.; Singh, R.; Dhiman, R. P2X7 Receptor in Multifaceted Cellular Signalling and Its Relevance as a Potential Therapeutic Target in Different Diseases. *Eur. J. Pharmacol.* **2021**, *906*, 174235. https://doi.org/10.1016/j.ejphar.2021.174235.

(10) Kopp, R.; Krautloher, A.; Ramírez-Fernández, A.; Nicke, A. P2X7 Interactions and Signaling – Making Head or Tail of It. *Front. Mol. Neurosci.* **2019**, *12*.

(11) Lara, R.; Adinolfi, E.; Harwood, C. A.; Philpott, M.; Barden, J. A.; Di Virgilio, F.; McNulty, S. P2X7 in Cancer: From Molecular Mechanisms to Therapeutics. *Front. Pharmacol.* **2020**, *11*, 793. https://doi.org/10.3389/fphar.2020.00793.

(12) Baudelet, D.; Lipka, E.; Millet, R.; Ghinet, A. Involvement of the P2X7 Purinergic Receptor in Inflammation: An Update of Antagonists Series since 2009 and Their Promising Therapeutic Potential. *Curr. Med. Chem.* **2015**, *22* (6), 713–729. https://doi.org/10.2174/0929867322666141212120926.

(13) Karasawa, A.; Kawate, T. Structural Basis for Subtype-Specific Inhibition of the P2X7 Receptor. *eLife* **2016**, *5*, e22153. https://doi.org/10.7554/eLife.22153.

(14) Allsopp, R. C.; Dayl, S.; Dayel, A. B.; Schmid, R.; Evans, R. J. Mapping the Allosteric Action of Antagonists A740003 and A438079 Reveals a Role for the Left Flipper in Ligand Sensitivity at P2X7 Receptors. *Mol. Pharmacol.* **2018**, *93* (5), 553–562. https://doi.org/10.1124/mol.117.111021.

(15) Bin Dayel, A.; Evans, R. J.; Schmid, R. Mapping the Site of Action of Human P2X7 Receptor Antagonists AZ11645373, Brilliant Blue G, KN-62, Calmidazolium, and ZINC58368839 to the Intersubunit Allosteric Pocket. *Mol. Pharmacol.* **2019**, *96* (3), 355–363. https://doi.org/10.1124/mol.119.116715.

(16) Allsopp, R. C.; Dayl, S.; Schmid, R.; Evans, R. J. Unique Residues in the ATP Gated Human P2X7 Receptor Define a Novel Allosteric Binding Pocket for the Selective Antagonist AZ10606120. *Sci. Rep.* **2017**, *7* (1), 725. https://doi.org/10.1038/s41598-017-00732-5.

(17) Stokes, L.; Jiang, L.-H.; Alcaraz, L.; Bent, J.; Bowers, K.; Fagura, M.; Furber, M.; Mortimore, M.; Lawson, M.; Theaker, J.; Laurent, C.; Braddock, M.; Surprenant, A. Characterization of a Selective

and Potent Antagonist of Human P2X7 Receptors, AZ11645373. *Br. J. Pharmacol.* **2006**, *149* (7), 880–887. https://doi.org/10.1038/sj.bjp.0706933.
(18) Alcaraz, L.; Baxter, A.; Bent, J.; Bowers, K.; Braddock, M.; Cladingboel, D.; Donald, D.; Fagura, M.; Furber, M.; Laurent, C.; Lawson, M.; Mortimore, M.; McCormick, M.; Roberts, N.; Robertson, M. Novel P2X7 Receptor Antagonists. *Bioorg. Med. Chem. Lett.* **2003**, *13* (22), 4043–4046. https://doi.org/10.1016/j.bmcl.2003.08.033.
(19) Michel, A. D.; Clay, W. C.; Ng, S. W.; Roman, S.; Thompson, K.; Condreay, J. P.; Hall, M.; Holbrook, J.; Livermore, D.; Senger, S. Identification of Regions of the P2X(7) Receptor That Contribute to Human and Rat Species Differences in Antagonist Effects. *Br. J. Pharmacol.* **2008**, *155* (5), 738–751. https://doi.org/10.1038/bjp.2008.306.
(20) Michel, A. D.; Ng, S.-W.; Roman, S.; Clay, W. C.; Dean, D. K.; Walter, D. S. Mechanism of Action of Species-Selective P2X(7) Receptor Antagonists. *Br. J. Pharmacol.* **2009**, *156* (8), 1312–1325. https://doi.org/10.1111/j.1476-5381.2009.00135.x.
(21) Albert, J.; Cadena, J. M.; Granell, J. Cyclopalladation of the Primary Amine (*R*)-(+)-1-(1-Naphthyl)Ethylamine: A New Resolving Agent for Monodentate Phosphines. *Tetrahedron Asymmetry* **1997**, *8* (7), 991–994. https://doi.org/10.1016/S0957-4166(97)00087-6.
(22) Coles, S. J.; Gale, P. A. Changing and Challenging Times for Service Crystallography. *Chem. Sci.* **2012**, *3* (3), 683–689. https://doi.org/10.1039/C2SC00955B.
(23) He, Y.; Wang, B.; Dukor, R. K.; Nafie, L. A. Determination of Absolute Configuration of Chiral Molecules Using Vibrational Optical Activity: A Review. *Appl. Spectrosc.* **2011**, *65* (7), 699–723. https://doi.org/10.1366/11-06321.
(24) Merten, C.; Golub, T. P.; Kreienborg, N. M. Absolute Configurations of Synthetic Molecular Scaffolds from Vibrational CD Spectroscopy. *J. Org. Chem.* **2019**, *84* (14), 8797–8814. https://doi.org/10.1021/acs.joc.9b00466.
(25) Polavarapu, P. L.; Santoro, E. Vibrational Optical Activity for Structural Characterization of Natural Products. *Nat. Prod. Rep.* **2020**, *37* (12), 1661–1699. https://doi.org/10.1039/D0NP00025F.
(26) O'Connor, T. J.; Mai, B. K.; Nafie, J.; Liu, P.; Toste, F. D. Generation of Axially Chiral Fluoroallenes through a Copper-Catalyzed Enantioselective β-Fluoride Elimination. *J. Am. Chem. Soc.* **2021**, *143* (34), 13759–13768. https://doi.org/10.1021/jacs.1c05769.
(27) Devlin, F. J.; Stephens, P. J.; Cheeseman, J. R.; Frisch, M. J. Ab Initio Prediction of Vibrational Absorption and Circular Dichroism Spectra of Chiral Natural Products Using Density Functional Theory: α-Pinene. *J. Phys. Chem. A* **1997**, *101* (51), 9912–9924. https://doi.org/10.1021/jp971905a.
(28) Polavarapu, P. L.; Covington, C. L. Comparison of Experimental and Calculated Chiroptical Spectra for Chiral Molecular Structure Determination. *Chirality* **2014**, *26* (9), 539–552. https://doi.org/10.1002/chir.22316.
(29) Debie, E.; De Gussem, E.; Dukor, R. K.; Herrebout, W.; Nafie, L. A.; Bultinck, P. A Confidence Level Algorithm for the Determination of Absolute Configuration Using Vibrational Circular Dichroism or Raman Optical Activity. *Chemphyschem Eur. J. Chem. Phys. Phys. Chem.* **2011**, *12* (8), 1542–1549. https://doi.org/10.1002/cphc.201100050.
(30) Barczyk, A.; Roy, H. B.-L.; Jouy, N.; Renault, N.; Hottin, A.; Millet, R.; Vouret-Craviari, V.; Adriouch, S.; Idziorek, T.; Dezitter, X. Flow Cytometry: An Accurate Tool for Screening P2RX7 Modulators. *Cytometry A* **2020**, *n/a* (n/a). https://doi.org/10.1002/cyto.a.24287.
(31) Caseley, E. A.; Muench, S. P.; Baldwin, S. A.; Simmons, K.; Fishwick, C. W.; Jiang, L.-H. Docking of Competitive Inhibitors to the P2X7 Receptor Family Reveals Key Differences Responsible for Changes in Response between Rat and Human. *Bioorg. Med. Chem. Lett.* **2015**, *25* (16), 3164–3167. https://doi.org/10.1016/j.bmcl.2015.06.001.
(32) Špačková, A.; Vávra, O.; Raček, T.; Bazgier, V.; Sehnal, D.; Damborský, J.; Svobodová, R.; Bednář, D.; Berka, K. ChannelsDB 2.0: A Comprehensive Database of Protein Tunnels and Pores in AlphaFold Era. *Nucleic Acids Res.* **2024**, *52* (D1), D413–D418. https://doi.org/10.1093/nar/gkad1012.

(33) Agranat, I.; Caner, H.; Caldwell, J. Putting Chirality to Work: The Strategy of Chiral Switches. *Nat. Rev. Drug Discov.* **2002**, *1* (10), 753–768. https://doi.org/10.1038/nrd915.
(34) Sali, A.; Blundell, T. L. Comparative Protein Modelling by Satisfaction of Spatial Restraints. *J. Mol. Biol.* **1993**, *234* (3), 779–815. https://doi.org/10.1006/jmbi.1993.1626.
(35) McNutt, A. T.; Francoeur, P.; Aggarwal, R.; Masuda, T.; Meli, R.; Ragoza, M.; Sunseri, J.; Koes, D. R. GNINA 1.0: Molecular Docking with Deep Learning. *J. Cheminformatics* **2021**, *13* (1), 43. https://doi.org/10.1186/s13321-021-00522-2.
(36) Krieger, E.; Vriend, G. YASARA View - Molecular Graphics for All Devices - from Smartphones to Workstations. *Bioinforma. Oxf. Engl.* **2014**, *30* (20), 2981–2982. https://doi.org/10.1093/bioinformatics/btu426.